EARTH SURFACE PROCESSES AND LANDFORMS
Earth Surf. Process. Landforms **43**, 1183–1194 (2018)

Published online 2 March 2018 in Wiley Online Library
(wileyonlinelibrary.com) DOI: 10.1002/esp.4290

Strong variation in weathering of layered rock maintains hillslope-scale strength under high precipitation

Jennifer Von Voigtlander,[1,2] Marin K. Clark,[1]* Dimitrios Zekkos,[3] William W. Greenwood,[3] Suzanne P. Anderson,[4] Robert S. Anderson[5] and Jonathan W. Godt[6]

[1] Department of Earth and Environmental Sciences, University of Michigan, Ann Arbor, MI USA
[2] Schlumberger Limited, Houston, TX USA
[3] Department of Civil and Environmental Engineering, University of Michigan, Ann Arbor, MI USA
[4] Department of Geography and INSTAAR, University of Colorado, Boulder, CO USA
[5] Department of Geological Sciences and INSTAAR, University of Colorado, Boulder, CO USA
[6] Natural Hazards Mission Area, Landslide Hazards Program, US Geological Survey, Denver, CO USA

Received 7 June 2016; Revised 8 June 2017; Accepted 8 November 2017

*Correspondence to: Marin K. Clark, Department of Earth and Environmental Sciences, University of Michigan, Ann Arbor, MI 48109, USA. E-mail: marinkc@umich.edu

ESPL
Earth Surface Processes and Landforms

ABSTRACT: The evolution of volcanic landscapes and their landslide potential are both dependent upon the weathering of layered volcanic rock sequences. We characterize critical zone structure using shallow seismic V_p and V_s profiles and vertical exposures of rock across a basaltic climosequence on Kohala peninsula, Hawai'i, and exploit the dramatic gradient in mean annual precipitation (MAP) across the peninsula as a proxy for weathering intensity. Seismic velocity increases rapidly with depth and the velocity–depth gradient is uniform across three sites with 500–600 mm/yr MAP, where the transition to unaltered bedrock occurs at a depth of 4 to 10 m. In contrast, velocity increases with depth less rapidly at wetter sites, but this gradient remains constant across increasing MAP from 1000 to 3000 mm/yr and the transition to unaltered bedrock is near the maximum depth of investigation (15–25 m). In detail, the profiles of seismic velocity and of weathering at wet sites are nowhere monotonic functions of depth. The uniform average velocity gradient and the greater depths of low velocities may be explained by the averaging of velocities over intercalated highly weathered sites with less weathered layers at sites where MAP > 1000 mm/yr. Hence, the main effect of climate is not the progressive deepening of a near-surface altered layer, but rather the rapid weathering of high permeability zones within rock subjected to precipitation greater than ~1000 mm/yr. Although weathering suggests mechanical weakening, the nearly horizontal orientation of alternating weathered and unweathered horizons with respect to topography also plays a role in the slope stability of these heterogeneous rock masses. We speculate that where steep, rapidly evolving hillslopes exist, the sub-horizontal orientation of weak/strong horizons allows such sites to remain nearly as strong as their less weathered counterparts at drier sites, as is exemplified by the 50°–60° slopes maintained in the amphitheater canyons on the northwest flank of the island.

KEYWORDS: critical zone; regolith formation; shallow seismic profiles; slope stability; Hawai'i; basalt weathering

Introduction

The critical zone (CZ) is defined as near-surface environments on Earth (national Research Council [NRC], 2001), in which life is supported, and where natural hazards that threaten human lives and infrastructure occur. Subsurface heterogeneities and environmental gradients characterizing the CZ result from complex interactions of physical, chemical, and biological processes responding to tectonic, climatic, and anthropogenic forcings over time (Anderson *et al.*, 2007; Brantley *et al.*, 2007; Ritter *et al.*, 2011; Riebe *et al.*, 2017). Our understanding of CZ structure and strength remains inadequate to incorporate in quantitative models of landscape evolution and in robust assessment of slope hazards. As such, development of future models depends on our ability to extrapolate outcrop-scale observations to geomorphically relevant scales, which in part requires understanding how individual environmental factors affect CZ evolution (Anderson *et al.*, 2007; Brantley *et al.*, 2007; Holbrook *et al.*, 2014; Riebe *et al.*, 2017).

Weathering and fracturing dramatically reduce the mechanical strength of materials in the CZ, ultimately breaking bedrock down to transportable material (Selby, 1980; Anderson and Anderson, 2010). CZ thickness, degree of weathering and strength reduction are typically thought to be proportional to precipitation and to its residence time in the near surface (e.g. Hoek and Brown, 1980, 1997; Rahardjo *et al.*, 2004; Brantly and White, 2009; Lebedeva and Brantly, 2013; Anderson *et al.*, 2013; Rempe and Dietrich, 2014). Hence erosion rates are associated with regional climate (Dixon *et al.*, 2009; Ritter *et al.*, 2011; Murphy *et al.*, 2016). Weathering-related weakening is often conceptually simplified as the top-down alteration of unweathered bedrock, which progressively extends rock

damage to greater depths as weathering progresses (e.g. Anderson *et al.*, 2007; Brantley and Lebedeva, 2011). However, variability in initial permeability structure, fracture density or weathering susceptibility may complicate this simple concept (e.g. Mohamed *et al.*, 2008; Goodfellow *et al.*, 2014). Accelerated weathering may occur in high permeability or densely fractured zones, which will produce a strength profile that differs from that resulting from simple top-down weathering into a homogeneous substrate.

The most distinct subdivision within the CZ is that between altered and unaltered bedrock, or in engineering terms, the distinction between soil and rock. Strength values range over an order of magnitude across this continuum, which is typically observed in the upper tens of meters of the Earth's surface. The upper fully altered, or 'damaged', layer consists of mobile regolith (i.e. material that is free to move and may be transported diffusively, often simply called soil) below which intact or immobile regolith includes a continuum from saprolite to weathered and fractured rock (Anderson *et al.*, 2007; Anderson *et al.*, 2013). The variability in the mechanical strength of immobile regolith is one of the least understood aspects of the near-surface rock profile (Hachinohe *et al.*, 1999; Moon and Jayawardane, 2004; Bursztyn *et al.*, 2015), where weathering and discontinuities of the rock mass reduce intact rock strength in rock mass classification schemes (e.g. Hoek and Brown, 1997). Because detachment of variably damaged rock from intact regolith contributes to sediment production by various means (fluvial, glacial, mass wasting), the mechanical evolution of the intact regolith should influence physical erosion rates and thus play a key role in both landscape evolution and hillslope stability.

Although the strength of weathered and fractured rock masses are described by classification schemes employed by the geotechnical engineering community (e.g. Hoek and Brown, 1980; Hoek, 1994), we lack systematic studies that integrate weathering processes with rock strength evolution. This fact limits our ability to extrapolate observed CZ structure to geologically relevant time and spatial scales. Presumably, as precipitation exerts primary control on mechanical properties of the CZ through rock weathering, this may be quantified through spatial trends in rock strength reflected in seismic velocity profiles. As yet, interpretation of CZ architecture from geophysical imaging is a developing science (Parsekian *et al.*, 2015). The extreme precipitation gradient across the northern district of Kohala peninsula on the Island of Hawai'i provides an ideal natural laboratory to investigate the long-term effects of precipitation on CZ structure from P- and S-wave velocity profiles obtained across a uniform basalt lithology. In this study, we performed shallow seismic surveys and examined nearby vertical exposures of the rock structure. Using seismic velocity as a proxy for mechanical strength, these observations guide a conceptual model of CZ evolution as a function of mean annual precipitation (MAP) for Kohala. This model can be generally applied to sites in which weathering potential is stratified by either initial lithologic characteristics or subsequent fracturing. We can also relate heterogeneous weathering processes and rock strength to models of slope stability and the maintenance of unique and dramatic steep walled canyons in this setting, which challenges recent assertions of climate-modulated rock weakening as a primary control on river incision in this environment (Murphy *et al.*, 2016).

Geologic Setting

The Kohala Volcano is the oldest major shield volcano on the Island of Hawai'i, emerging above sea level roughly 500 000 years ago (Spengler and Garcia, 1988) (Figure 1). Pleistocene age volcanic rocks exposed in this region belong to either the older Pololu volcanics (460–260 ka) (McDougall, 1969; McDougall and Swanson, 1972; Spengler and Garcia, 1988) or the younger Hawi volcanics (230–120 ka) (McDougall, 1969; McDougall and Swanson, 1972; Wolfe and Morris, 1996; Chadwick *et al.*, 2003). Both of these systems produced basaltic lava flows, but they differ in both structural and chemical characteristics typical of a shield building sequence. The tholeiitic Pololu volcanics are primarily pahoehoe flows, which are vesicular and have a ropey, rolling surface texture and commonly contain lava tubes. The younger, alkalic flows of the Hawi volcanics are a'a flows with a significantly rougher surface morphology and lower vesicularity compared to the Pololu volcanics (Spengler and Garcia, 1988). Because the initial flow structure and texture likely influenced weathering and strength profiles, we restricted our data collection to locations on the Pololu volcanics. Minimal erosion of the original shield surface also makes it an ideal site in which to isolate weathering gradients as a function of precipitation.

The maximum elevation in Kohala exceeds 1600 m, producing a dramatic orographic rain shadow from south-westerly trade winds striking the north-eastern flank of the volcano. The orography is reflected in an order of magnitude difference in MAP across the peninsula, ranging from 200 mm/yr on the western side to 4000 mm/yr in the east (Giambelluca *et al.*, 2013) (Figure 1). While the precipitation gradient presumably grew as volcanic topography accumulated, and varied during glacial/interglacial periods (Chadwick *et al.*, 2003; Porter, 2005), perceptible geographic variations in precipitation have been interpreted to exist for at least the last 50 000 years (Porter, 2005). In this study, we use variations in MAP across similarly aged basalts as a proxy for the expected weathering progression. In most cases, we were able to conduct surveys near human-made or natural exposures of the CZ from which we could evaluate both the degree of weathering and support our interpretation of the seismic velocity structure.

Methods

Few surveys characterize variations in CZ weathering profiles across environmental gradients. Because small-scale variability in lithology, mineralogy, topography, and erosion produce heterogeneous weathering profiles, it remains a challenge to produce field data relevant to hillslope and watershed scales. Techniques such as augering and trenching are depth limited, and the expense of drilling to greater depths generally prohibits coverage over broad areas. Geophysical techniques, such as shallow seismic methods using short arrays and active sources, are ideal for hillslope scale studies because they are inexpensive and can be deployed in remote and steep topography (Parsekian *et al.*, 2015; St Clair *et al.*, 2015). Shallow seismic profiling also offers advantages compared to other methods because it is non-invasive and quantification of material properties from seismic velocities has been established by the geotechnical engineering community. Two-dimensional (2D) surveys can be used to construct and constrain layer boundaries, such as the thickness of various regolith layers and the depth to unweathered bedrock, as well as to characterize horizontal variability in subsurface structure, material properties and fluid saturation (e.g. Barton, 2007; Befus *et al.*, 2011; Greenwood *et al.*, 2015).

Subsurface velocities are related to material density and stiffness of intact rock, but are also very sensitive to the density of fractures, joint roughness and void spaces at a range of scales. An increase in porosity and a decrease in density and elastic moduli are associated with weathering degree and

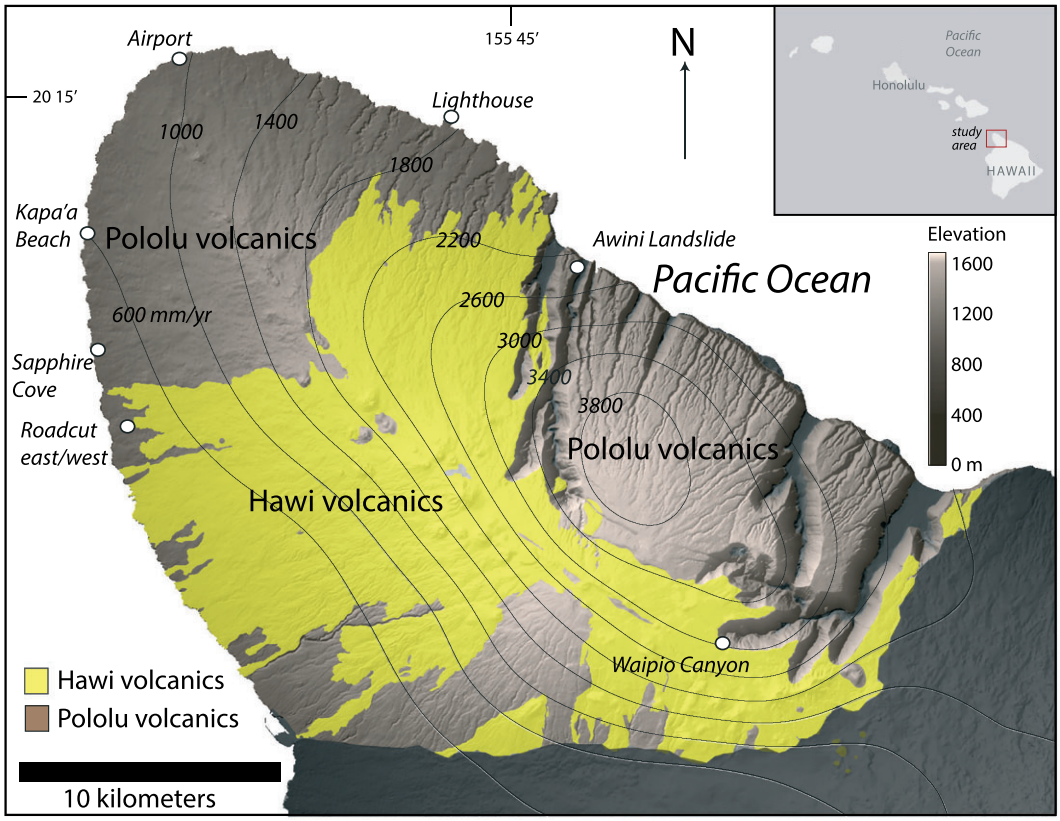

Figure 1. Geologic map of Kohala district of Hawai'i with seismic survey locations (dots). Mean annual precipitation (MAP) in mm/yr is derived from Giambelluca *et al.* (2013). [Colour figure can be viewed at wileyonlinelibrary.com]

contribute to a decrease of seismic velocities as weathering progresses (Barton, 2007). The number, size and infilling of cracks, and the numbers and size of voids also affect the velocity of wave propagation through the material (e.g. Stanchits *et al.*, 2006; Clarke and Burbank, 2011). Using P- and S-wave velocity as a proxy for weathering, climatic control on rock strength reduction can be quantitatively determined based on developed relationships between P- and S-wave velocities and strength, most commonly, unconfined compressive strength (UCS) (e.g. Gupta and Rao, 1998; Tugrul and Zarif, 2000; Sarno *et al.*, 2010).

First-arrival seismic refraction studies are a common method to infer the P-wave velocity structure of the shallow subsurface depth and velocity by inferring the rate of wave propagation along various ray paths from travel-time curves (Burger *et al.*, 2006). Tomographic methods produce 2D velocity profiles from which layering and material boundaries, such as the regolith-bedrock contact, can be identified (Stokoe and Santamarina, 2000; Burger *et al.*, 2006; Stanchits *et al.*, 2006; Befus *et al.*, 2011; Holbrook *et al.*, 2014). Down-going seismic waves that encounter a higher velocity layer underlying a lower velocity layer are refracted along and back up toward the surface, and thus seismic refraction surveys only accurately characterize subsurface stratigraphy in which velocity increases with depth (Stokoe and Santamarina, 2000). In the opposite case, a lower velocity layer underlying a higher velocity layer would refract waves away from the surface and would not be observed, thus the inability of P-wave refraction studies to identify low-velocity layers in an alternating sequence is a limitation of the technique.

Established techniques using surface waves (i.e. Rayleigh waves) to interpret S-wave velocity profiles (a body wave) have advanced in reliability in recent years (e.g. Foti *et al.*, 2009; Yoon and Rix, 2009; Pelekis and Athanasopoulos, 2011). These methods rely on the dispersive properties of Rayleigh waves, which refers to different wavelength (or frequency) waves traveling at different velocities, and their relationship to S-wave velocities. Where S-wave velocities change with depth, small wavelength (high frequency) waves sample shallow regions, whereas longer wavelengths (lower frequency) sample greater depths (e.g. Stokoe and Santamarina, 2000). The multichannel analysis of surface waves (MASW) method has been used to generate extensive data in a variety of natural and synthetic materials (e.g. Greenwood *et al.*, 2015; Duffy *et al.*, 2014). MASW employs a linear array of geophones and an impulsive source, or harmonic oscillator, to generate and measure Rayleigh waves. Dispersion is characterized and then used as part of a forward-modeling inversion approach to evaluate the S-wave velocity profile (Park *et al.*, 1998, 1999). It should be noted that surface wave methods, in general, have difficulty identifying velocity changes in thin layers at depth because increasingly lower frequency waves are relied upon to sample greater depths, resulting in greater 'averaging' of the subsurface in deeper parts of the profile (Stokoe and Santamarina, 2000). The inversion of surface wave dispersion into an S-wave velocity profile has no unique solution much like other geophysical methods (Foti *et al.*, 2009). This means that care must be taken, or model restrictions through complementary data must be collected to ensure that a solution that is representative of the site conditions is realized during the inversion procedure.

Seismic survey parameters and processing

Seismic profiles for both P- and S-wave velocities were recorded using a 16-channel Geometrics ES-3000 portable seismometer. Total survey length, as well as the velocity structure, determines the depth of investigation. Shallow profiles provided high resolution that can be compared to vertical rock

sequence exposures, while deeper sections provided information about depth to unweathered bedrock. The details of each survey design and modeling parameters are reported in the Supporting Information.

P-wave lines were recorded with either 4.5 or 40 Hz geophones, using a sledge hammer source (3.6 and 7.2 kg) to strike a 10 cm square, 2.5 cm thick metal or 15 cm square, 5 cm thick plastic plate. Geophone spacing varied between 1 and 3 m and shots were recorded in between geophones and as off-end strikes were recorded at 1 and 5 m intervals, producing total line lengths of 15 to 45 m. This resulted in typical P-wave models with a depth of investigation of 4 to 18 m (see Supporting Information).

We compute 2D P-wave velocity profiles using a linearized tomographic inversion, suitable for sites with complicated velocity structures and lateral velocity variations. This technique can be applied to areas with less distinct velocity contrasts as well as to areas of layered subsurface with sharp velocity contrasts. We assume an initial linear velocity profile and apply a ray-tracing algorithm to determine the fastest theoretical travel times (i.e. the first arrival) for each receiver given specified survey geometry. The difference between the observed and theoretical travel times for the ray paths is described by the root mean square error (RMSE) and provides a means to assess the validity of the inferred velocity models. Choice of initial velocity model on the resulting theoretical travel time curve has a small effect on the final velocity model, the variability of which we estimate to be 40 m/s (one-standard deviation) (Supporting Information). Theoretical travel time curves are generated from the initial velocity model and then iteratively changed in order to find a best fit between theoretical and observed travel times. Seisimager software module Pickwin and Plotrefa were used to produce time travel curves and to invert the waveform interpretation for a velocity structure of the shallow subsurface respectively (OYO Corporation, 2006; Hayashi and Takahasi, 2001).

Seismic profiles for S-wave velocity were measured using, initially, the same survey lines as the P-wave profiles, then were shifted by one sensor spacing (1–3 m) in the direction of the array in order to produce a 2D array (Supporting Information). Rayleigh waves were measured using 4.5 Hz geophones spaced at 1 to 3 m and impulsive sources were generated using a 3.6 to 7.2 kg hammer on a 15 cm square, 5 cm thick plastic plate (Supporting Information). The source was input at an offset of about 15–20% of the total array length to avoid near-field effects (Yoon and Rix, 2009). Shots were stacked 5–10 times to improve signal-to-noise ratio.

Surface wave measurements were processed using the common mid-point cross-correlation (CMPCC) procedure (Hayashi and Suzuki, 2004). CMPCC is an extension of the traditional one-dimensional (1D) and 2D MASW procedures (Park *et al.*, 1998; Xia *et al.*, 2000) and is intended to improve spatial resolution in the final profile (Hayashi and Suzuki, 2004). Both fundamental and higher-mode Rayleigh waves were considered in the analysis. Higher-mode Rayleigh waves arise in specific subsurface conditions, such as low-velocity layers interbedded with high-velocity layers (Stokoe *et al.*, 1994). Utilizing higher-modes in these site conditions is necessary to improve resolution and depth of investigation, stabilize inversion results, and realize complex subsurface velocity structures (Xia *et al.*, 2003). An initial velocity structure was assumed and the dispersion curves were back-calculated and compared with the measured dispersion curves. The S-wave velocity profile was then iteratively adjusted until the best dispersion curve match was achieved. This is often done using a least squares method. The best dispersion curve matches were used to generate the final S-wave velocity profiles.

Seismic Velocity Profiles

The comparison of velocity profiles as a function of MAP is used to interpret changes in CZ architecture as a function of weathering, assuming precipitation as a proxy for weathering degree. P-wave velocity cross-sections derived from the linearized tomographic inversion are presented for eight study sites. In addition, S-wave profiles from three of the eight sites accompany the P-wave data. Results are summarized in two groups: dry sites (500–600 mm/yr MAP) and wet sites (> 1000 mm/yr MAP). At most sites, vertical exposures of 4 to 10 m height in the vicinity of the seismic survey are used to compare velocity measurements to rock fracture patterns and field observations of weathering degree.

Dry sites (500–600 mm/yr MAP)

Surveys were conducted at three sites on the dry (leeward) side of the Kohala peninsula with similar MAP (500–600 mm/yr) (Figures 1 and 2). Variable geophone spacing for overlapping profiles produced both high resolution in the near surface (4 m depth) as well as greater depth of investigation (18 m maximum) at lower resolution.

P-wave data obtained using 1.0 and 1.5 m spaced lines generally show steep velocity gradients in the upper few meters of the section, below which velocities are constant or increase more gradually with increasing depth (Figure 2). The slowest velocity layer (300–500 m/s) is 0–2 m thick and is underlain by velocities of 500 to 1500 m/s extending to 3–4 m depth. Modeled P wave velocities (V_p) are laterally discontinuous nearest the surface, consistent with the patchy exposure of corestones interspersed with saprolite and sandy soil. Greater line spacing (2.5–3 m) results in models with a more gradual increase in velocity over this same depth and velocity interval compared to the 1 and 1.5 m spaced lines. This likely occurs because V_p velocities are averaged or smoothed out and these models have higher modeled misfits to the data as a result of the wider geophone spacing (Figure 2, Supporting Information). At the sites with the greatest depth of investigation (18 m), maximum velocities reach 3500–3800 m/s at 7–15 m depth.

A single S-wave profile for the dry sites shows similarly steep S-wave velocity (V_s) versus depth gradients as the P-wave data (Figure 2). Within the upper 3 m, the lowest S-wave velocity is 200–300 m/s. However, this near surface lower V_s velocity layer is laterally discontinuous and reaches higher velocities of 500 m/s toward the north end of the line. Like the P-wave data, along-strike variability in the near surface V_s velocities is consistent with surface exposures of both rock and soil. Near the maximum depth of investigation (12 m) V_s velocities reach 650–700 m/s.

Wet sites (> 1000 mm/yr MAP)

Four P-wave surveys were collected at sites with variable MAP on the wet, windward side of the island (MAP ~ 1000-3000 mm/yr) (Figures 1 and 3), and two S-wave profiles were collected at sites with 1000 mm/yr MAP (Airport) and 1500 mm/yr MAP (Lighthouse) (Figure 4). As with the dry sites, variable geophone spacing for individual profiles produced higher resolution in the near surface with closer geophone spacing (4 m depth) as well as greater depth of investigation using larger geophone spacings (25 m maximum depth). Two of the surveys were collected at coastal sites adjacent to sea cliff exposures (Airport and Lighthouse). Two other surveys were collected within the steep amphitheater canyons on the northeast side of the peninsula (Awini landslide and Waipio Canyon).

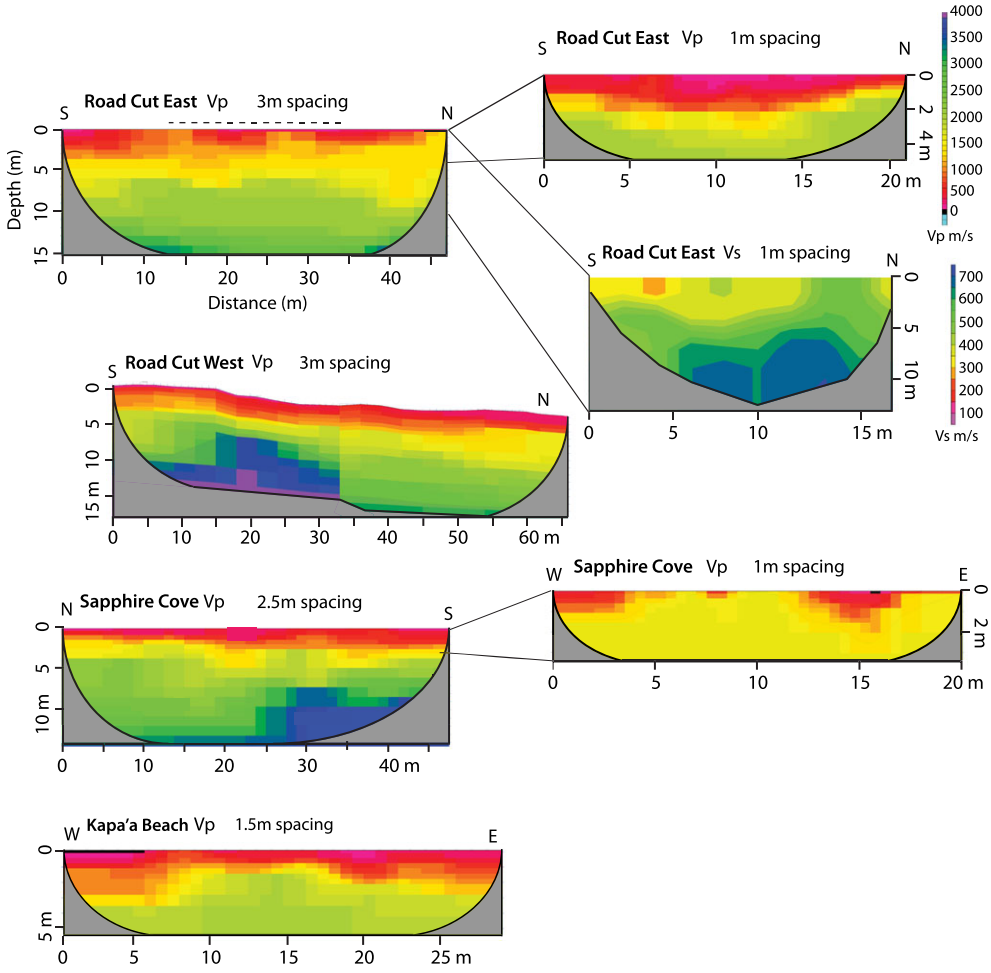

Figure 2. P- and S-wave velocity models for dry sites (MAP 500–600 mm/yr). Multiple profiles at a single site display results from different geophone spacings and dashed lines represent survey overlap. Smaller geophone spacing resolves greater detail near the surface of the profile (right panels). [Colour figure can be viewed at wileyonlinelibrary.com]

Similar to the dry sites, the P-wave surface layer of the wet sites is associated with steeper velocity/depth gradients in survey lines with 1 and 1.5 m spacing compared to larger spacings. However, the surface V_p velocity layer (300–500 m/s) is thicker (5–10 m compared to 0–2 m for the dry sites, with the exception of the Awini landslide) (Figure 3). Below this surface layer, V_p velocity increases with depth more gradually compared to the dry sites. Maximum V_p velocities reach 1200 to 1500 m/s at the maximum depth of investigation (12–15 m depth) and are much lower than the velocities at equivalent depths at dry sites. The exception is the Awini landslide site where the profile was collected across a landslide scar. Here, the surface layer (V_p = 300–500 m/s) is thin to non-existent and V_p velocities below this horizon (800–1200 m/s) at depths of up to 3 m are higher than at equivalent depths on the other three wet sites. Presumably the landslide removed a lower V_p velocity surface layer.

S-wave profiles show stratification with prominent high and low velocity horizons that are laterally discontinuous (Figure 4). At the Airport site (MAP ~1000 mm/yr), the upper seismic stratum displays V_s velocities as low as 100–200 m/s in a discontinuous layer ~2 m thick. This surface horizon is underlain by a zone of fast V_s seismic velocities (400–600 m/s) extending down to 4 m depth. A prominent subsurface low-velocity horizon (V_s = 100–200 m/s) is modeled between 4 and 8 m depth. Similarly, the Lighthouse profile (MAP ~ 1500 mm/yr) shows stratification with a low velocity surface horizon underlain at depth with discontinuous high velocity horizons at 3–7 m depth, and low velocity horizons between 5 and 10 m depth. In both profiles, V_s velocities increase at greater depths (> 10 m) to 450 m/s at 14 m depth to more than 550–600 m/s at the maximum depth of investigation (25 m). The alteration of low to high V_s velocity in the upper 10 m of the profile corresponds to intervals of greater/lesser weathering in sea cliff exposures adjacent to the profiles (Figure 4).

Seismic Characterization of the CZ

Rock weathering at the dry site Road Cut East (Figure 2), previously described by Goodfellow *et al.* (2014), provides a weathering classification scheme for the seismic velocity model. The classification scheme extracted from this comparison was used at the other dry sites (MAP 500–600 mm/yr), but cannot account for the observed layering of material properties observed for wet sites (MAP > 1000 mm/yr). Presumably, the presence of soft, weathered material lowers the seismic velocities, resulting in a different characterization of the CZ for wet sites and is readily observed as low velocity horizons on S-wave profiles (Figure 4).

Dry sites (MAP 500–600 mm/yr)

We superimpose the geochemical weathering profile characterized by Goodfellow *et al.* (2014) on the Road Cut East 1 m V_p profile (Figure 5). There is a good correspondence between the uppermost velocity layer (V_p = 300–500 m/s) and

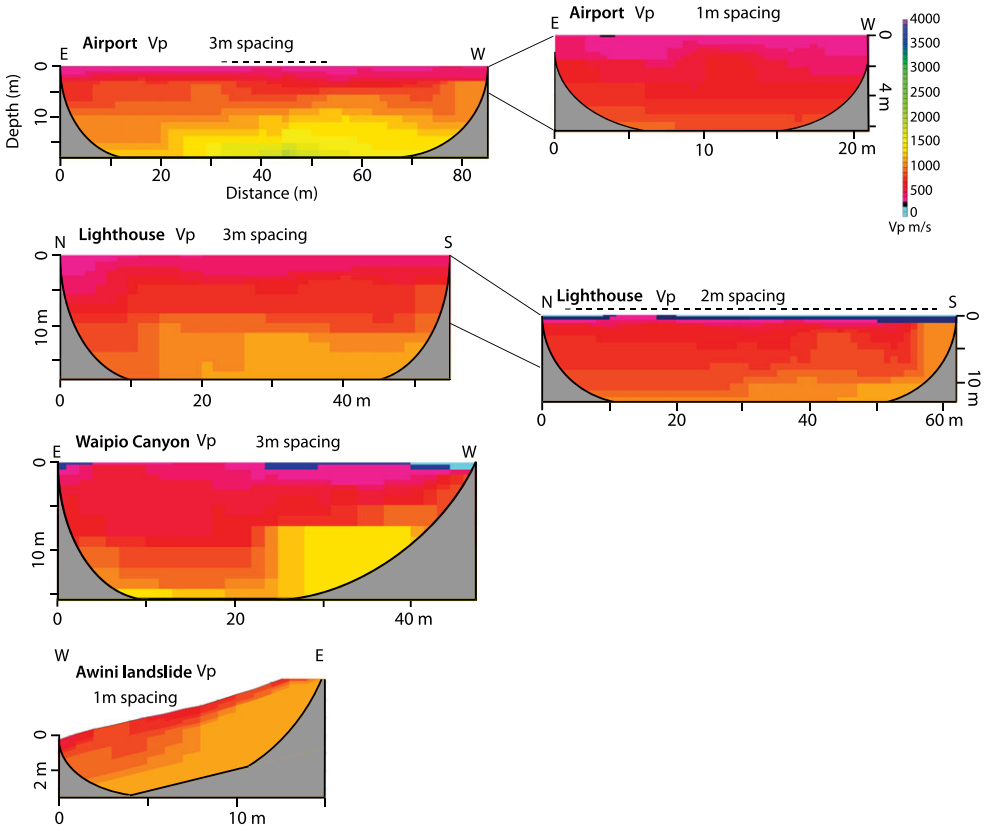

Figure 3. P-wave velocity models for wet sites (MAP 1000–3000 mm/yr). Sites with multiple profiles vary in geophone spacings and dashed lines represent survey overlap. Shorter geophone spacing resolves greater detail near the surface of the profile. [Colour figure can be viewed at wileyonlinelibrary.com]

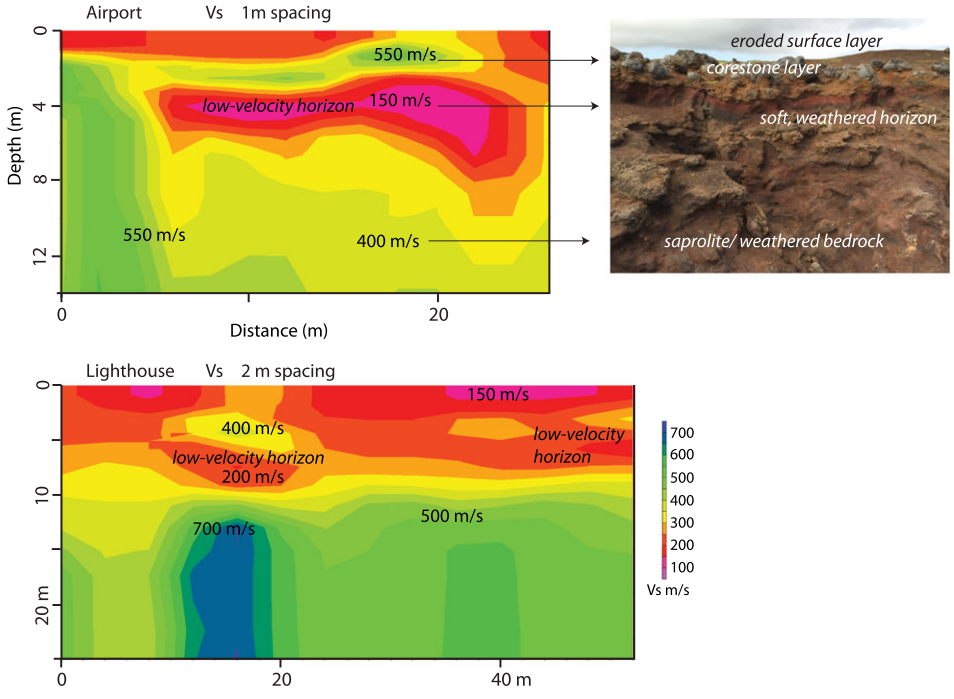

Figure 4. S-wave velocity models for two wet sites. The low-velocity horizon at ~4 m depth corresponds to a soft, weathered horizon observed in the sea cliff (top right) adjacent to the seismic survey. [Colour figure can be viewed at wileyonlinelibrary.com]

a layer identified as 'soil (clast-rich)' (all weathering descriptions in quotations are those of Goodfellow *et al.* [2014] and were determined based on chemical depletion measured from samples as well as outcrop characteristics). The next lower layer is a mixture of 'saprolite' and 'slightly weathered rock', where we observe V_p = 500–1500 m/s. Below 2 m depth, the outcrop is characterized mainly as fractured, 'unweathered rock' and corresponds to P-wave velocities of 1500 to 2000 m/s and V_s = 500 m/s. This 'unweathered' distinction by Goodfellow *et al.* (2014) is made on the basis of chemical

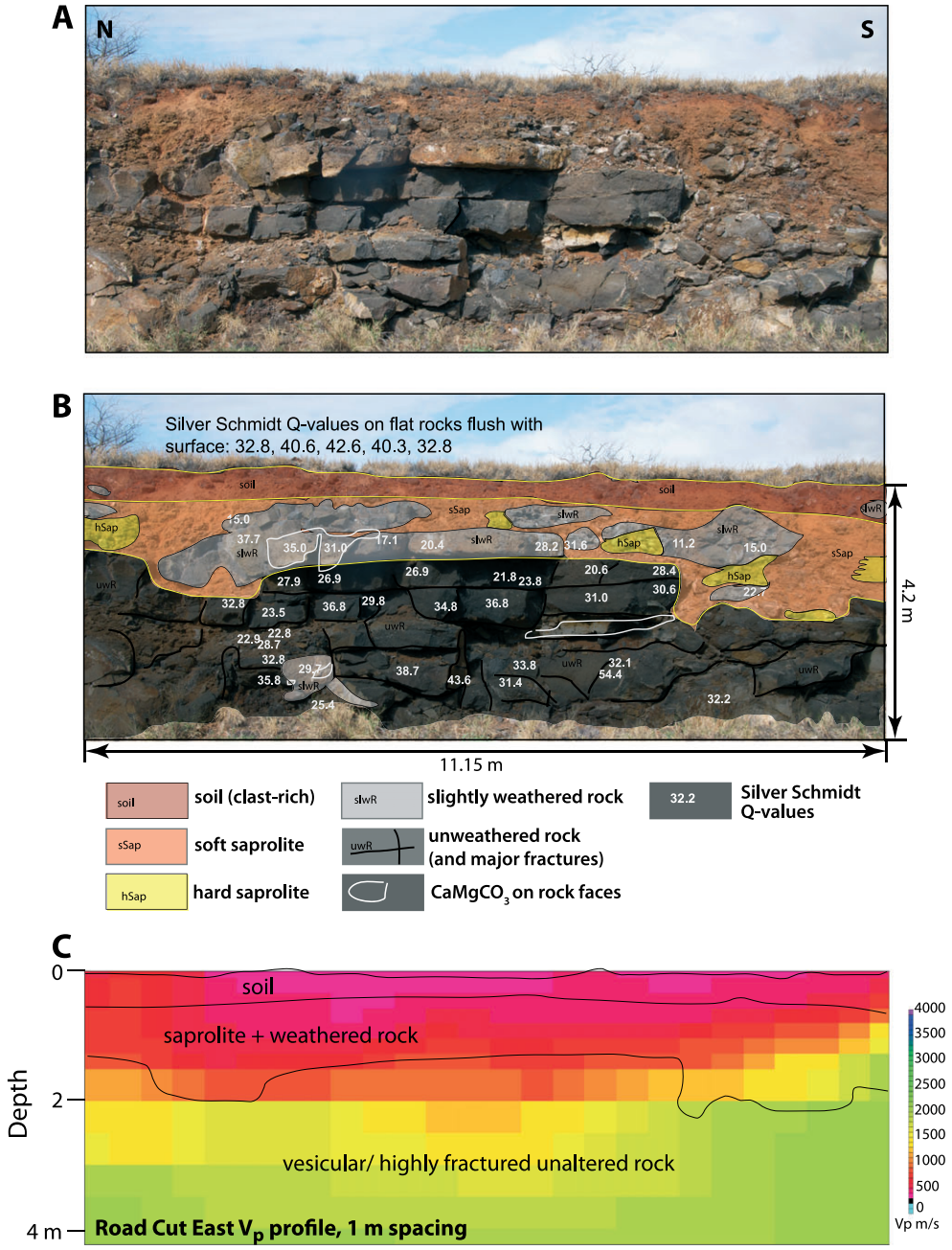

Figure 5. P-wave velocity model of Road Cut East site compared to a weathering profile interpretation and Silver Schmidt© hammer rebound measurements. (A) Photograph of section exposure from Road Cut East seismic site (Figures 1 and 2), which was collected parallel to and 5 m back from the photographed road cut. (B) Weathering interpretation and descriptions of Goodfellow *et al.* (2014) for the same road cut. Numbers in white indicate hammer *Q* values (average, $n = 10$) measured on the outcrop. (C) Select portion of velocity profile from Road Cut East, 1 m line (Figure 2), which overlaps road cut section. Black lines represent interpreted soil, saprolite + weathered rock, and vesicular/highly fractured, unaltered rock layers interpreted from the road cut section. [Colour figure can be viewed at wileyonlinelibrary.com]

alteration, and we note that this layer contains rock that is intensely fractured and commonly has a vesicular texture, and thus is physically weathered.

We collected Silver Schmidt© hammer measurements on the outcrop as well, and found that measurable rebound values could only be obtained on rocks classified by Goodfellow as 'slightly weathered rock' and 'unweathered rock' in the road cut, as well as on corestones exposed at the surface along the seismic profile. The softer material of the saprolite and soil result in null rebound values. Rebound measurements, or '*Q*-values', vary from a mean of 24.1 ± 9.1 for 'slightly weathered rock' to 30.9 ± 7.2 for 'unweathered rock', which is consistent with a lower velocity for layers classified by Goodfellow as 'slightly weathered rock' compared to 'unweathered rock'. Slightly weathered to unweathered blocks make up a larger proportion of each layer of increasing seismic velocity, which further suggests that the seismic velocity reflects the average properties of a layer. We also note that hammer rebound values tend to increase downward, similar to the observed increase in V_p seismic velocity. At greater depth (i.e. below the exposure in the road cut), we observe an increase in velocity to a maximum V_p = 3000 m/s at 12 m depth (Figure 2, Road Cut West 3-m spacing line). At these same depths, V_s increases to 700 m/s.

While these observed maximum seismic velocities (V_p = 3000 m/s and V_s = 700 m/s) are lower than typically reported for basalt (V_p = 5400–6400 m/s and V_s = 2700–3200 m/s) (Barton, 2007), we suggest that vesicularity and fracturing present in the young basalts we measured, as well as the low confining stress present in near surface conditions, yield lower

maximum V_p velocities for this study site compared to other CZ investigations (Befus *et al.*, 2011; Holbrook *et al.*, 2014; Parsekian *et al.*, 2015). Three lines of evidence lead us to interpret the maximum seismic velocities in Kohala as representing chemically unaltered, but fractured or vesicular rock at depth. First, our maximum V_s velocities are equivalent to previously reported 'unweathered basalt' S-wave velocities for the Kohala peninsula (670 m/s, Wong *et al.*, 2011) based on a greater depth of investigation (up to 70 m depth) than presented in this study. The relative consistency of V_p and V_s as a function of depth for a constant V_p/V_s ratio, suggests that V_p and V_s are well correlated in this environment (Figure 6) and gives us confidence in extrapolating the V_s interpretation to the V_p profiles. Second, in top flow basalts, vesicles formed during magma degassing generate pore space, and micro-/macro-cracks are generated during cooling, but these features diminish as the rock is subsequently buried to greater depths. Vesicles and cracks have been shown to dramatically reduce seismic velocities compared to massive basalts. For example, Al-Harthi *et al.* (1999) demonstrated an exponential decrease in V_p over the range from 2 to 6.5 km/s as a function of porosity for basalt cores from Saudi Arabia (at zero confining pressure). Cerney and Carlson (1999) measured a range in V_p for basalt cores IDP Hole 990A on the southeast Greenland margin during Ocean Drilling Program Leg 163, from 2.2 to 6.5 km/s, reflecting differences in down-hole rock properties, mainly mineralogy and porosity (~2–7% porosity). Third, we measured 1D P-wave profiles on a historic flow with pahoehoe textures in order to evaluate the initial V_p velocity of the Pololu volcanics just following crystallization and prior to any further weathering at the Earth's surface. Observed velocities were even slower despite the absence of chemical weathering (300–1000 m/s, Supporting Information).

As a result, we classify P-wave velocity through CZ material at dry sites as follows: soil (< 500 m/s), saprolite/slightly weathered rock (500–1500 m/s), and chemically unaltered, fractured basalt (> 1500 m/s) reaching a maximum of 3000 m/s (Figures 2 and 5). Similarly, soil V_s velocities range from as low as 100–200 m/s, increase to 200–500 m/s for saprolite/weathered rock, and reach values of unaltered basalt at > 500 m/s. The soil layer is interpreted to range from 0 to 2 m thick, consistent with the surface exposure of corestones and rock along surveyed profiles where the soil layer is absent. The thickness of the saprolite/weathered layer averages 2–4 m. We interpret unaltered basalt at depths of 2 to 4 m for the road cut sites, 5–6 m depth at Sapphire Cove and 2–4 m at Kapa'a Beach. It is an important point that the Kohala CZ is mechanically 'pre-weathered' in its initial state by processes associated with magma degassing and cooling due to vesicles and fractures. Thus we relate the changes in velocity for chemically unaltered rock, from 1500 to 3000 m/s, to likely be related to closing of vesicular pore space and cracks, which are present in near surface flow layers.

Wet sites (MAP > 1000 mm/yr)

For wet sites, we observe interbedded horizons of stiff and soft material below the surface soil horizon. Where sea cliffs are present along studied profiles, this interbedding is present down to the base of the cliff, which correlates with a stiff, resistant layer. In outcrop, the layers commonly contain variably weathered fractured bedrock or corestones; some horizons are quite intact with only incipient weathering on fracture or joint surfaces. Although V_p and V_s seismic velocities were lower at the surface in the wet sites than the dry sites, outcrops reveal weathered rock and corestones present throughout the profile. Thus, the classification scheme derived from Goodfellow *et al.* (2014) that we employed for the dry sites was not directly applicable to velocity models obtained on the wet sites. Instead, we suggest that the observed soft layers in the subsurface lower the average V_p and V_s velocity for a given model horizon (Figure 4). This relationship is observed at the Airport and Lighthouse site, where S-wave velocity data resolves low velocity horizons several meters in thickness that are 3 to 10 meters deep from the surface. We note that the thickness and velocity of the low-velocity horizon are not uniquely constrained. For example, the dispersion data could also match a model with a thicker low-velocity layer of somewhat higher velocity. At the Airport site, the low V_s velocity layer corresponds with the outcrop of a reddish, soft saprolite horizon interpreted to have soil-like material properties, which underlies a more resistant layer of fractured bedrock and abundant corestones. The overall effect of this layered structure is to lower the average P- and S-wave velocities over a larger depth interval.

For wet sites, the interpreted near-surface soil thicknesses were similar to dry sites (1–2 m generally, although less than 1 m at the Awini landslide site) (Figures 4 and 5). However, the

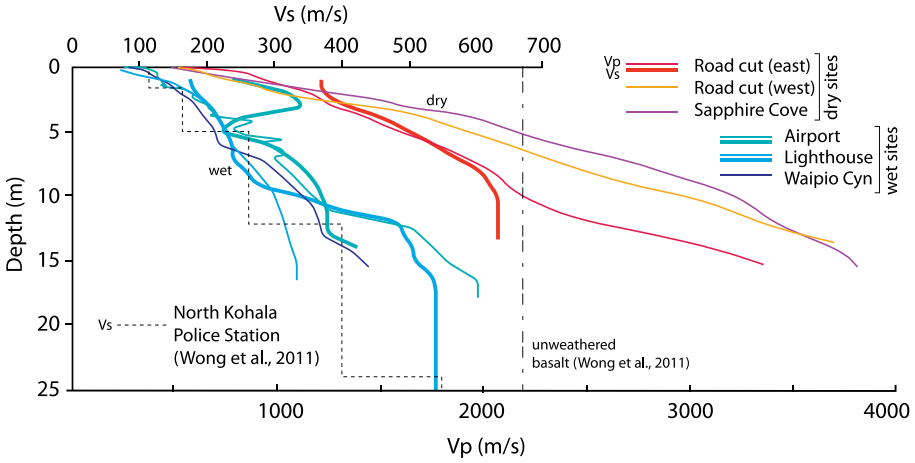

Figure 6. Averaged P- and S-wave velocities as a function of depth (thick and thin lines respectively). Dry sites (500–600 mm/yr) mean annual precipitation (MAP) show rapid increases in velocity with depth. These profiles reach unweathered basalt velocities (Wong *et al.*, 2011) at ~4–10 m depth. Sites with 1000 mm/yr MAP and greater display more gradual increase in velocity with depth and do not vary significantly with precipitation. The average velocity–depth gradient is in agreement with previous S-wave profiles in Kohala on Pololu units (Wong *et al.*, 2011). Average velocities of these high precipitation sites approach our interpreted 'unaltered basalt' values within the maximum depth of investigation (15–25 m) but do not reach the 'unweathered basalt' values proposed by Wong *et al.* (2011). [Colour figure can be viewed at wileyonlinelibrary.com]

average V_p and V_s velocity of this layer is lower than on the dry sites (Figure 6), which may be due to higher clay content associated with more pronounced chemical mineral alteration. Below the soil, we interpret a zone of interbedded slightly weathered basalt and saprolite with more deeply weathered layers. This interval typically extends to depths of 15 to 25 m depth, which is the maximum depth of investigation for our profiles. These depths correspond to P-wave velocities of 1200 to 1700 m/s and S-wave velocities of 500 to 700 m/s, which overlaps with the lowest velocities that we associate with unaltered basalt at dry sites and with the S-wave velocities of 'unweathered basalt' reported by Wong *et al.* (2011) (670 m/s), but do not reach the maximum velocities that we observe on the dry sites.

Throughout Kohala, the groundwater table lies at or within a few meters of sea level (Oki *et al.*, 1999). Thus, groundwater may influence the P-wave velocity for some of our sites collected near sea level (Sapphire Cove, Kapa'a Beach, Upolo Airport and the Lighthouse). Based on studies of analogous rocks, water saturation could perturb the V_p velocities by several hundred meters per second. For example, a study of vesicular basalts from the western Snake River Plain reproduced bulk modulus predictions from physical models for fluid substitution in porous rocks (Gassmann's relation) for frequencies less than 20 Hz (Adam and Otheim, 2013), and suggest a 500 m/s increase in V_p at low confining pressures (~3 MPa) for water-saturated basalts with 10–20% porosity. Weathering can also influence fluid substitution through the introduction of clay, and could produce both increasing and decreasing trends in V_p (up to ±400 m/s) for increasing degrees of saturation depending on the lithology, pore space, and clay concentration (Karakul and Ulusay, 2013).

However, two lines of evidence give us confidence in our assertion that the water table for sites near sea level did not significantly influence our interpretations. First, we do not see a systematic change in V_p at sea level (the estimated groundwater level) for sites near the coast compared to those at higher altitudes (Figure 6). Second, the groundwater table does not affect V_s and we observe similar average gradients for V_p and V_s for dry and wet sites respectively and a constant V_p/V_s ratio, suggesting that the V_p profiles are not perturbed by the water table (Figure 6).

Discussion

Precipitation, as a proxy for chemical weathering, appears to influence the depth and structure of the CZ across the Kohala peninsula. Dry sites have thin regolith (less than 4 m), with shallow depth-to-unaltered bedrock. Where observed, the interpreted depth to unaltered, fractured and vesicular bedrock (V_p >1500 m/s and V_s> 500 m/s seismic velocities) occurs at depths of between 2 and 6 m. By comparison, wet sites have thicker, highly-weathered regolith and do not reach the same maximum velocities as dry sites at a depth of investigation 18 m for P-wave profiles and 25 m for S-wave profiles. Because the highest interpreted velocities at the maximum depth of investigation were lower than the maximum unaltered bedrock values on the dry sites, we speculate that weathered horizons are interbedded with less weathered horizons (or even unweathered) to at least 25 m depth.

Dry sites and wet sites have distinct velocity–depth gradients (Figure 6). These gradients are bimodal, clustering around one value for dry sites (MAP ~500–600 mm/yr) and decreasing more than three-fold to another value for wet sites (MAP ~1000–3000 mm/yr) with a V_p/V_s ratio of 3.2. The velocity–depth gradients do not systematically decrease with increasing precipitation among wet sites. One possible explanation is that the initial permeability structure of the basalt flow sequence dictates the weathering susceptibility in the upper tens of meters of the shield surface (Oki *et al.*, 1999; Goodfellow *et al.*, 2014). Chemical weathering rates in Hawai'i are observed to be non-linear, where above a precipitation threshold weathering rates increase dramatically compared with drier sites but do not increase further with increasing rainfall (Porder *et al.*, 2007). We speculate that where MAP exceeds 1000 mm/yr in this particular environment, a weathering threshold is reached above which high-permeability basalt horizons undergo rapid weathering and reach soil-like material properties, and contrast with other less permeable layers that weather only slightly and retain rock-like material properties. We hypothesize that the absence of further reduction in the velocity gradient with yet greater precipitation reflects a threshold beyond which further weathering (and associated softening/weakening) of high-permeability zones to soil-like properties cannot occur (i.e. the rock has weathered to residual soil) and that weathering of low-permeability zones are insensitive to the differences in precipitation observed here. This suggests that the governing factor on the reduction of seismic velocity at the wet sites is the rapid weathering of high permeability horizons within a layered sequence.

An interbedded weathering profile in which highly weathered and nearly unweathered layers are intercalated provides an alternative to a simple top-down weathering model, and provides insight into the weathering process and its effects on the near surface strength profile (Figure 7). While interbedding of stiff and soft materials lowers the average P- and S-wave velocities as evaluated by surface-based methods, the average strength of the near surface profile and its effect on slope stability likely depends on both the ratio of end-member materials and the orientation of layers with respect to hillslope aspect. Generally, the introduction of weak layers within a heterogeneous rock mass results in a back-calculated lower strength for landslides within the rock mass, when the geometry (orientation, thickness, and depth) of the weak layer dominates the shear resistance of the landslide mass (e.g. Duffaut, 1981; Marinos and Hoek, 2001; Marinos, 2010). However, the average strength is likely dependent on the ratio of intact strength of the end member materials (Mohamed *et al.*, 2008; Tziallas *et al.*, 2013) and the disturbance/orientation of the layering (Marinos, 2010). At our sites, the nearly horizontal

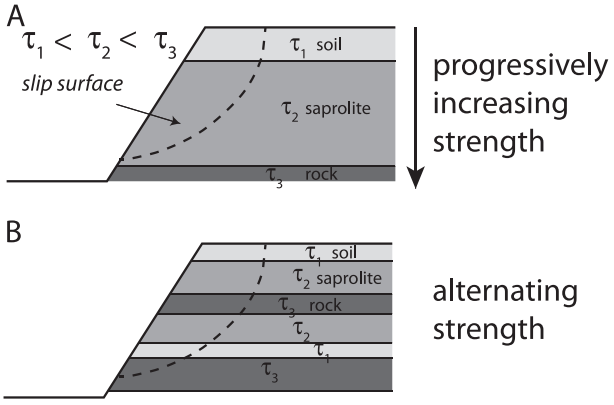

Figure 7. Hypothetical slip-surfaces for slopes with two different strength profiles. The back-calculated shear strength will depend on the weighted average of material strength, τ, along the slip surface. Thus the relative differences in bulk strength between the two profiles will depend on the relative differences in τ between the different layers, and the surface area of each layer along the failure plane. In Kohala, we suggest that the observed horizontal layers of slightly weathered to unweathered rock in the near-surface profile may contribute significantly to the strength of steep hillslopes.

layering of stiff, slightly weathered to unweathered basalts within the Pololu flows on Kohala has the following effects: (a) To restrict failure surfaces (landslides) to shallow depths in the more weathered layers only; and (b) for deeper failure surfaces that intersect both the unweathered and weathered layers, a back-calculated, or estimated strength based on an observed slope failure, would yield a higher average strength than would be estimated without such layering (Figure 7). Within sedimentary rock sequences, sub-horizontal layering of strong and softer layers produces smaller critical failure surfaces than would have been otherwise expected for uniform rock mass properties using theoretical predictions of slope failures (e.g. Zekkos *et al.*, 2008).

The steep walls of dramatic canyons provide insight to the hillslope-scale rock strength properties of the wet side of Kohala. These steep-sided, amphitheater canyons common to the windward facing slopes (e.g. Lamb *et al.*, 2007) are among the most striking features of the Hawaiian Islands. Here the 60° and steeper hillslopes that define the amphitheater heads and walls of the canyons persist despite precipitation rates of over 4000 mm/yr. We speculate that the high hillslope-scale rockmass strength implied by these steep hillslopes reflects two attributes of the setting: the interbedding of highly weathered intervals with largely unweathered layers that remain stiff and strong, and the sub-horizontal dip of the bedding, which is therefore nearly orthogonal to the steeply inclined hillslopes. As such, the link between precipitation and weathering of heterogeneous rock profiles and its relationship to various geomorphic processes, including landsliding, is a potential avenue for future investigation.

While the influence of physical erosion rate on chemical weathering is well recognized (e.g. West *et al.*, 2005; Ferrier and Kirchner, 2008; Dixon *et al.*, 2012; Larsen *et al.*, 2014), the role of chemical weathering on the strength profile of a rock sequence potentially influences the nature and rate of physical erosion processes (e.g. Molnar *et al.*, 2007; Sarno *et al.*, 2010; Han *et al.*, 2014). The Kohala peninsula in Hawai'i is an extreme example of what is likely a common weathering-strength phenomenon. In any heterogeneous rock mass in which spatial variation in material properties such as permeability and weathering potential exist, pronounced layering at the scale of the hillslopes can produce heterogeneous weathering profiles and mechanical properties that vary non-monotonically with depth. For instance, the most productive aquifers in Hawai'i are found in sequences with permeable layers between lava flows that direct water flow (Oki *et al.*, 1999). Sedimentary sequences, metamorphic terrains and highly tectonized environments where rock fracturing may influence the weathering potential are likely to display similar weathering trajectories. Because the structure of the subsurface dictates the mechanical behavior, especially in weathered and weak rock masses (Hoek and Brown, 1997; Marinos and Hoek, 2001; Marinos, 2010), the presence of weak horizons and their orientation relative to the topographic surface must be taken into account when estimating bulk rock strength relevant to both the study of landscape evolution and the assessment of geologic hazards. The generation of strong regional strength anisotropy created by non-monotonic depth profiles of weathering in some geologic settings contrasts with a simple top-down weathering-related strength profile and may invalidate simple correlations between precipitation, chemical weathering and rock strength at scales relevant to physical erosion processes (e.g. Murphy *et al.*, 2016).

Conclusions

We hypothesize that the stratified permeability structure of the Kohala basalt sequence has produced a hillslope-scale anisotropic rock mass strength profile. Low-seismic velocity horizons correspond to exposures of soil-like material and deeply weathered saprolite. The presence of interbedded, highly weathered horizons to depths of tens of meters may explain the decrease in P- and S-wave velocity–depth gradients for sites >1000 mm/yr MAP and the uniformity of these profiles with increasing precipitation. A model of rock strength that is derived from intercalated weak and strong layers differs fundamentally from that expected from simple top-down propagation of a weathering front, which otherwise would be predicted to progressively weaken hillslopes with increasing precipitation. Instead, under circumstances in which the layering is orthogonal to hillslopes, hillslope-scale strength anisotropy might maintain rather than reduce hillslope stability. These results emphasize the need to understand weathering-related evolution of the full rock–strength profile, acknowledging that anisotropy can also influence properties of the hillslope-scale rock mass and may be an important feature of CZ architecture in many geologic settings.

Acknowledgements—This work was supported by a collaborative award from the USGS National Earthquake Hazards Reduction Program (NEHRP) grants G15AP00007 and G15AP00008 to M. Clark, R. Anderson and S. Anderson, Rackham Graduate Student travel grants (University of Michigan), the Scott Turner fund (Department of Earth and Environmental Sciences, University of Michigan), discretionary funding from the University of Michigan, a CIRES Visiting Faculty Fellowship from CU Boulder to M. Clark and partial funding from the National Science Foundation (NSF), Division of Civil and Mechanical Systems under Grant No. CMMI-1362975 to D. Zekkos, and EAR-1331828 to S. Anderson. Any opinions, findings, conclusions and recommendations expressed in this paper are those of the authors, including the views of the US Geological Survey, but do not necessarily reflect the views of the other funding agencies. Any use of trade, firm, or product names is for descriptive purposes only and does not imply endorsement by the US Government. We thank Katherine Lowe and Mitsuhito Hirose for field assistance during the seismic data acquisition and Lou Derry for logistical guidance.

References

Adam L, Otheim T. 2013. Elastic laboratory measurements and modeling of saturated basalts. *Journal of Geophysical Research, Solid Earth* **118**: 1–12. https://doi.org/10.1002/jgrb.50090.

Al-Harthi AA, Al-Amri RM, Shehata WM. 1999. The porosity and engineering properties of vesicular basalt in Saudi Arabia. *Engineering Geology* **54**(3): 313–320. https://doi.org/10.1016/S0013-7952(99)00050-2.

Anderson RS, Anderson SP. 2010. *Geomorphology: The Mechanics and Chemistry of Landscapes*. Cambridge University Press: Cambridge.

Anderson RS, Anderson SP, Tucker GE. 2013. Rock damage and regolith transport by frost: an example of climate modulation of the geomorphology of the critical zone. *Earth Surface Processes and Landforms* **38**: 299–316. https://doi.org/10.1002/esp.3330.

Anderson SP, von Blanckenburg F, White AF. 2007. Physical and chemical controls on the critical zone. *Elements* **3**: 315–319.

Barton N. 2007. *Rock Quality, Seismic Velocity, Attenuation and Anisotropy*. CRC Press: Boca Raton, FL.

Befus KM, Sheehan AF, Leopold M, Anderson SP, Anderson RS. 2011. Seismic constraints on critical zone architecture, Boulder Creek Watershed, Colorado. *Vadose Zone Processes* **10**(3): 915–927. https://doi.org/10.2136/vzj2010.0108.

Brantley SL, Goldhaber MB, Ragnarsdottir KV. 2007. Crossing disciplines and scales to understand the critical zone. *Elements* **3**(5): 307–314.

Brantley SL, White AF. 2009. Approaches to modeling weathered regolith. *Reviews in Mineralogy and Geochemistry* **70**(1): 435–484. https://doi.org/10.2138/rmg.2009.70.10.

Brantley SL, Lebedeva M. 2011. Learning to read the chemistry of regolith to understand the critical zone. *Annual Review of Earth and Planetary Sciences* **39**: 387–416. https://doi.org/10.1146/annurev-earth%20040809-152321.

Burger HR, Sheehan AF, Jones CH. 2006. *Introduction to Applied Geophysics: Exploring the Shallow Subsurface*. WW Norton: New York.

Bursztyn N, Pederson JL, Tressler C, Mackley RD, Mitchell KJ. 2015. Rock strength along a fluvial transect of the Colorado Plateau – quantifying a fundamental control on geomorphology. *Earth and Planetary Science Letters* **429**: 90–100. https://doi.org/10.1016/j.epsl.2015.07.042.

Cerney B, Carlson RL. 1999. The effect of cracks on the seismic velocities of basalt from site 990, southeast Greenland margin. In Proceedings of the Ocean Drilling Program. *Scientific Results* **163**: 29–35.

Clarke BA, Burbank DW. 2011. Quantifying bedrock-fracture patterns within the shallow subsurface: implications for rock mass strength, bedrock landslides, and erodability. *Journal of Geophysical Research* **116**: F04009. https://doi.org/10.1029/2011JF001987.

Chadwick OA, Gavenda RT, Kelly EF, Ziegler D, Olson CG, Elliott WC, Hendricks DM. 2003. The impact of climate on the biogeochemical functioning of volcanic soils. *Chemical Geology* **202**: 193–221.

Dixon JL, Heimsath AM, Amundson R. 2009. The critical role of climate and saprolite weathering in landscape evolution. *Earth Surface Processes and Landforms* **34**(11): 1507–1521.

Dixon JL, Hartshorn AS, Heimsath AM, DiBiase RA, Whipple KX. 2012. Chemical weathering response to tectonic forcing: a soils perspective from the San Gabriel Mountains, California. *Earth and Planetary Science Letters* **323**: 40–49.

Duffaut P. 1981. Structural weaknesses in rocks and rock masses: tentative classification and behaviour. In *Proceedings of the International Society for Rock Mechanics*.

Duffy B, Campbell J, Finnemore M, Gomez C. 2014. Defining fault avoidance zones and Associated geotechnical properties using MASW: a case study on the Springfield Fault, New Zealand. *Engineering Geology* **183**: 216–229.

Ferrier KL, Kirchner JW. 2008. Effects of physical erosion on chemical denudation rates: a numerical modeling study of soil-mantled hillslopes. *Earth and Planetary Science Letters* **272**(3): 591–599.

Foti S, Comina C, Boiero D, Socco LV. 2009. Non-uniqueness in surface-wave inversion and consequences on seismic site response analyses. *Soil Dynamics and Earthquake Engineering* **29**(6): 982–993.

Giambelluca TW, Chen Q, Frazier AG, Price JP, Chen YL, Chu PS, Eischeid JK, Delparte DM. 2013. Online rainfall atlas of Hawai'i. *Bulletin of the American Meteorological Society* **94**(3): 313–316.

Goodfellow BW, Chadwick OA, Hilley GE. 2014. Depth and character of rock weathering across a basaltic hosted climosequence on Hawai'i. *Earth Surface Processes and Landforms* **39**(3): 381–398.

Greenwood W, Zekkos D, Sahadewa A. 2015. Spatial variation of shear wave velocity of waste materials from surface wave measurements. *Journal of Environmental and Engineering Geophysics* **20**(4): 287–301.

Gupta AS, Rao KS. 1998. Index properties of weathered rocks: inter-relationships and applicability. *Bulletin of Engineering Geology and the Environment* **57**(2): 161–172.

Hachinohe S, Hiraki N, Suzuki T. 1999. Rates of weathering and temporal changes in strength of bedrock of marine terraces in Boso Peninsula, Japan. *Engineering Geology* **55**: 29–43.

Han J, Gasparini NM, Johnson JP, Murphy BP. 2014. Modeling the influence of rainfall gradients on discharge, bedrock erodibility, and river profile evolution, with application to the Big Island, Hawai'i. *Journal of Geophysical Research - Earth Surface* **119**(6): 1418–1440.

Hayashi K, Takahashi T. 2001. High resolution seismic refraction method using surface and borehole data for site characterization of rocks. *International Journal of Rock Mechanics and Mining Sciences* **38**(6): 807–813.

Hoek E. 1994. Strength of rock and rock masses. *ISRM News Journal* **2**(2): 4–16.

Hoek E, Brown ET. 1980. Empirical strength criterion for rock masses. *Journal of Geotechnical and Geoenvironmental Engineering* **106**: 15715.

Hoek E, Brown ET. 1997. Practical estimates of rock mass strength. *International Journal of Rock Mechanics and Mining Sciences* **34**(8): 1165–1186.

Holbrook SW, Riebe CS, Elwaseif M, Hayes JL, Basler-Reeder K, Harry DL, Malazian A, Dosseto A, Hartsough PC, Hopmans JW. 2014. Geophysical constraints on deep weathering and water storage potential in the southern Sierra Critical Zone Observatory. *Earth Surface Processes and Landforms* **39**: 366–380. https://doi.org/10.1002/esp.3502.

Hayashi K, Suzuki H. 2004. CMP cross-correlation analysis of multichannel surface wave data. *Exploration Geophysics* **35**: 7–13.

Karakul H, Ulusay R. 2013. Empirical correlations for predicting strength properties of rocks from P-wave velocity under different degrees of saturation. *Rock mechanics and rock engineering* **46**(5): 981–999.

Lamb MP, Howard AD, Dietrich WE, Perron JT. 2007. Formation of amphitheater headed valleys by waterfall erosion after large-scale slumping on Hawai'i. *Geological Society of America Bulletin* **119**(78): 805–822.

Larsen IJ, Almond PC, Eger A, Stone JO, Montgomery DR, Malcolm B. 2014. Rapid soil production and weathering in the Southern Alps, New Zealand. *Science* **343**(6171): 637–640.

Lebedeva MI, Brantley SL. 2013. Exploring geochemical controls on weathering and erosion of convex hillslopes: beyond the empirical regolith production function. *Earth Surface Processes and Landforms* **38**(15): 1793–1807. https://doi.org/10.1002/esp.3424.

Marinos P, Hoek E. 2001. Estimating the geotechnical properties of heterogeneous rock masses such as flysch. *Bulletin of Engineering Geology and the Environment* **60**(2): 85–92.

Marinos V. 2010. New proposed GSI classification charts for weak or complex rock masses. *Bulletin of the Geological Society Greece, Proceedings of the 12th International Congress, Patras, Greece*, May.

McDougall I. 1969. Potassium–argon ages of lavas from the Hawi and Pololu Volcanic Series, Kohala Volcano, Hawaii. *Geological Society of America Bulletin* **80**: 2597–2600.

McDougall I, Swanson DA. 1972. Potassium–argon ages of lavas from the Hawi and Pololu Volcanic Series, Kohala Volcano, Hawaii. *Geological Society of America Bulletin* **83**: 3731–3738.

Mohamed Z, Mohamed K, Gye CC. 2008. Uniaxial compressive strength of composite rock material with respect to shale thickness ratio and moisture content. *Electronic Journal of Geotechnical Engineering* **13**: 1–10.

Molnar P, Anderson RS, Anderson SP. 2007. Tectonics, fracturing of rock, and erosion. *Journal of Geophysical Research - Earth Surface* **112**(F3): F03014.

Moon V, Jayawardane J. 2004. Geomechanical and geochemical changes during early stages of weathering of Karamu Basalt, New Zealand. *Engineering Geology* **74**: 57–72. https://doi.org/10.1016/j.enggeo.2004.02.002.

Murphy BP, Johnson JPL, Gaspirini NM, Sklar LS. 2016. Chemical weathering as a mechanism for the climatic control of bedrock river incision. *Nature* **532**: 223–227. https://doi.org/10.1038/nature17449.

National Research Council (NRC). 2001. *Basic Research Opportunities in Earth Science*. National Academy Press: Washington, DC 168 pp.

Oki DS, Gingerich SB, Whitehead RL. 1999. Hawaii. In *Ground Water Atlas of the United States, Segment 13, Alaska, Hawaii, Puerto Rico, and the US Virgin Islands: US Geological Survey Hydrologic Investigations Atlas*. USGS Office of Groundwater: Reston, VA 730-N, N12–N22, N36.

OYO Corporation. 2006. *SeisImager/2D manual, Version 3.2*. ftp://geom.geometrics.com/pub/seismic/SeisImager/Intallation_CD/SeisImager2D_Manu al/ [2015].

Park CB, Miller RD, Xia J. 1998. Imaging dispersion curves of surface waves on multi-channel record. In *Expanded Abstracts: 68th Annual International Meeting, Society of Exploration Geophysicists*, 1377–1380.

Park CB, Miller RD, Xia J. 1999. Multichannel analysis of surface waves. *Geophysics* **64**(3): 800–808.

Parsekian AD, Singha K, Minsley BJ, Holbrook WS, Slater L. 2015. Multiscale geophysical imaging of the critical zone. *Reviews of Geophysics* **53**: 1–26. https://doi.org/10.1002/2014RG000465.

Pelekis PC, Athanasopoulos GA. 2011. An overview of surface wave methods and a reliability study of a simplified inversion technique. *Soil Dynamics and Earthquake Engineering* **31**(12): 1654–1668.

Porter SC. 2005. Pleistocene snowlines and glaciation of the Hawaiian Islands. *Quaternary International* **138–139**: 118–128. https://doi.org/10.1016/j.quaint.2005.02.009.

Porder S, Hilley GE, Chadwick OA. 2007. Chemical weathering, mass loss, and dust inputs across a climate by time matrix in the Hawaiian Islands. *Earth and Planetary Science Letters* **258**(3): 414–427.

Rahardjo H, Aung KK, Leong EC, Rezaur RB. 2004. Characteristics of residual soils in Singapore as formed by weathering. *Engineering Geology* **73**(1): 157–169. https://doi.org/10.1016/j.enggeo.2004.01.002.

Riebe CS, Hahm WJ, Brantley SL. 2017. Controls on deep critical zone architecture: a historical review and four testable hypotheses. *Earth Surface Processes and Landforms* **42**(1): 128–156. https://doi.org/10.1002/esp.4052.

Rempe DM, Dietrich WE. 2014. A bottom-up control on fresh-bedrock topography under landscapes. *Proceedings of the National Academy of Sciences* **111**(18): 6576–6581. https://doi.org/10.1073/pnas.1404763111.

Ritter D, Kochel CR, Miller JR. 2011. *Process Geomorphology*, Fifth edn. New York: McGraw Hill.

Sarno A, Farah R, Hudyma N, Hiltunen DR. 2010. Relationships between Compression Wave Velocity and Unconfined Compression Strength for Weathered Florida Limestone. In GeoFlorida 2010 Advances in Analysis, Modeling and Design. ASCE: Reston, VA; 950–959.

Selby MJ. 1980. A rock mass strength classification for geomorphic purposes: with tests from Antarctica and New Zealand. *Zeitschrift für Geomorphologie* **24**: 31–51.

Spengler SR, Garcia MO. 1988. Geochemistry of the Hawi lavas, Kohala Volcano, Hawaii. *Contributions to Mineralogy and Petrology* **99**: 90–104.

Stanchits S, Vinciguerra S, Dresen G. 2006. Ultrasonic velocities, acoustic emission characteristics and crack damage of basalt and granite. *Pure and Applied Geophysics* **163**(5–6): 975–994.

St Clair J, Moon S, Holbrook WS, Perron JT, Riebe CS, Martel SJ, Carr B, Harman C, Singha K, Richter D d B. 2015. Geophysical imaging reveals topographic stress control of bedrock weathering. *Science* **350**: 534–538. https://doi.org/10.1126/science.aab2210.

Stokoe KH, II, Wright SG, Bay JA, Roesset JM. 1994. Characterization of geotechnical sites by SASW method. In *Geophysical Characterization of Sites*, Woods RD (ed). International Science: New York; 15–26.

Stokoe KH, Santamarina JC. 2000. Seismic-wave-based testing in geotechnical engineering. *Proceedings of the International Society for Rock Mechanics*.

Tugrul A, Zarif IH. 2000. The influence of weathering on the geological and geomechanical characteristics of a sandstone in Istanbul, Turkey. *Environmental and Engineering Geoscience* **6**(4): 403–412.

Tziallas GP, Saroglou H, Tsiambaos G. 2013. Determination of mechanical properties of flysch using laboratory methods. *Engineering Geology* **166**: 81–89.

West AJ, Galy A, Bickle M. 2005. Tectonic and climatic controls on silicate weathering. *Earth and Planetary Science Letters* **235**(1): 211–228.

Wolfe EW, Morris J. 1996. *Geologic map of the Island of Hawaii*. Miscellaneous investigations series map I-2524-A. US Geological Survey: Reston.

Wong IG, Stokoe KH, Cox BR, Yuan J, Knudsen KL, Terra F, Okubo P, Lin YC. 2011. Shear-wave velocity characterization of the USGS Hawaiian strong-motion network on the island of Hawaii and development of an NEHRP site-class map. *Bulletin of the Seismological Society of America* **101**(5): 2252–2269.

Xia J, Miller RD, Park CB, Ivanov J. 2000. Construction of 2-D vertical shear-wave velocity field by the multichannel analysis of surface waves technique. *Proceedings of the Symposium on the Application of Geophysics to Engineering and Environmental Problems, Arlington, VA*, 20–24 February; 1197–1206.

Xia J, Miller RD, Park CB, Tian G. 2003. Inversion of high frequency surface waves with fundamental and higher modes. *Journal of Applied Geophysics* **52**: 45–57.

Yoon S, Rix JG. 2009. Near-field effects on array-based surface wave methods with active sources. *Journal of Geotechnical and Geoenvironmental Engineering* **135**(3): 399–406.

Zekkos D, Cohen-Waeber J, Medley E, Jesionek K. 2008. Characterization of weak rock mass and geoengineering analyses for a canyon landfill in northern California. Paper #6.05a. *Proceedings of the 6th International Conference on Case Histories in Geotechnical Engineering, Arlington, VA*, 11–16 August 2007.

Supporting Information

Additional Supporting Information may be found online in the supporting information tab for this article.

Supplementary Figure 1. Example data from dry sites (Road Cut Site Line 2). A) Wave form data with first break pick assignments (red). Pink line represents the travel time curve. B) Observed versus theoretical travel time curves. C) Linearized model after 60 iterations with ray path coverage shown. Geophone array noted by arrows.

Supplementary Figure 2. Example data from wet sites (Lighthouse line 2). A) Wave form data with first break pick assignments (red). Pink line represents the travel time curve. B) Observed (blue) versus calculated (black) travel time curves from the linearized model. C) Linearized model with ray path coverage shown.

Supplementary Figure 3. Sensitivity analysis for Lighthouse site. A) Initial velocity profiles used in the sensitivity analysis. B) Calculated standard deviation of velocity for resulting models (ms) using the range of initial velocity models in A.

Supplementary Figure 4. 1D Vp profiles from historic flows (1859 A.D.) near Kiholo Bay, Hawaii. A) Example waveform data and first-break picks (red). Pink line denotes travel-time curve. B) Travel time curve for three repeat trials. Near surface velocity is equal to the inverse slope of linear time-distance segments and ranges from ~ 300 - 1000 m/s. C) Photograph of fresh lava surface at survey site.

Supplementary Figure 5. MASW survey and data from the Upolo airport site (wet). A) Schematic of 2D MASW testing setup showing location of geophones. Shot and geophone location were shifted by one sensor spacing (1 m) in the direction of the array. Each shifted geometry is shown adjacent to the previous geometry for illustrative purposes. B) Frequency-Phase velocity diagram (blue showing preferred phase velocity for each Rayleigh wave frequency, red points show selected dispersion points plotted in part C. C) Measured dispersion points from B and modeled dispersion curve.

Supplementary Figure 6. MASW survey and data from the Lighthouse airport site (wet). A) Schematic of 2D MASW testing setup showing location of geophones. Shot and geophone location were shifted by one sensor spacing (2 m) in the direction of the array. Each shifted geometry is shown adjacent to the previous geometry for illustrative purposes. B) Frequency-Phase velocity diagram (blue showing preferred phase velocity for each Rayleigh wave frequency, red points show selected dispersion points plotted in part C. C) Measured dispersion points from B and modeled dispersion curve.

Supplementary Figure 7. MASW survey and data from the Highway 270 road cut east site (dry). A) Schematic of 2D MASW testing setup showing location of geophones. Shot and geophone location were shifted by one sensor spacing (1 m) in the direction of the array. Each shifted geometry is shown adjacent to the previous geometry for illustrative purposes. B) Frequency-Phase velocity diagram (blue showing preferred phase velocity for each Rayleigh wave frequency, red points show selected dispersion points plotted in part C. C) Measured dispersion points from B and modeled dispersion curve.

Supplementary Table 1: Seismic survey sites

Supplementary Table 2: P wave seismic survey and model parameters

Supplementary Table 3: S wave seismic survey parameters